

Multi-Band Sensing in FR3 with Background Dense Multipath Components

Dexin Wang, Roberto Bomfin, Ahmad Bazzi, and Marwa Chafii

Abstract—Multi-band sensing has emerged as a key enabler of integrated sensing and communication (ISAC), one of the six primary usage scenarios defined for IMT-2030 (6G). The introduction of frequency range 3 (FR3, 7-24 GHz), comprising non-contiguous sub-bands across a wide frequency span, further reinforces the importance of multi-band operation. In such scenarios, frequency-dependent propagation effects that are collectively referred to as dense multipath components (DMC), including clutter, diffraction, and diffuse scattering, must be carefully considered. Building on prior literature and our experimental observations, this paper proposes a novel ISAC channel analysis tailored to multi-band sensing, based on a channel model with background DMCs. It also assesses the sensing trade-offs among sub-bands by analyzing Cramér-Rao bound (CRB)-based fundamental limits. Furthermore, a scalable multi-band estimator is proposed that resolves angular ambiguities arising from the grating lobes effect. Simulation results of the multi-band estimator demonstrate substantial gains in estimation accuracy and reductions in false alarm rate over single-band estimators operating on each constituent sub-band within the CRB-achieving regime. In a representative test case, the proposed estimator achieves reductions of 37.41% and 17.04% in the root mean squared error of delay estimation compared to single-band estimators operating at 8.75 GHz and 21.7 GHz, respectively.

Index Terms—multi-band sensing, integrated sensing and communication, localization, dense multipath components, ISAC, FR3, 6G

I. INTRODUCTION

Future 6G systems are envisioned to reliably facilitate novel applications that interact more deeply with the physical world, such as the Internet of Things, autonomous driving, extended reality, smart cities, digital twins [1], and radio maps for environment-aware communication [2]. Thus, to save resources in bandwidth, hardware, processing power, and energy while facilitating efficient operation of such a large number of devices, integrated sensing and communication (ISAC) has been proposed as one of the six key usage scenarios of IMT-2030 (6G) [3]–[6]. One type of ISAC is *communication-centric ISAC* [7], which investigates the problem of performing sensing via existing communication protocols and infrastructure [8], [9], including the allocated frequency bands. With the addition of frequency range 3 (FR3,

7-24 GHz) [10]–[12] and terahertz (THz) [13], future 6G systems will likely operate in a wide range of frequencies and even multiple sub-bands [14]. Hence, one interesting topic in 6G ISAC will undoubtedly be to perform multi-band sensing in FR3 using signals from communication protocols [15], [16].

A. Background Concepts and Related Works

Multi-band sensing is the technique of performing sensing across non-contiguous frequency bands. From the literature, some of the reasons for choosing multi-band sensing are as follows [17]–[20]. First, to achieve higher time resolution, a typical approach is to use a large bandwidth. Nevertheless, increasing bandwidth is often associated with higher hardware costs and greater algorithmic complexity. Second, the increased amount of sensing data implies a lower error probability. For example, if severe fading happens at a particular frequency band, information from other bands can still be used. For single-band ISAC systems, where ideal wideband sensing waveforms, such as radar chirps, are typically unavailable, the loss can be mitigated by using multi-band sensing. Third, by accounting for frequency dependence in the signal model, we can estimate more environmental parameters and obtain additional information on the target, such as size, material, or roughness, beyond Cartesian locations alone. Finally, since the frequency bands allocated to one operator are typically non-contiguous (especially in FR3, considering coexistence with other occupiers such as satellites [21]), multi-band sensing is a practical assumption considering ISAC applications.

Typical sensing processing in ISAC literature relies on parameter estimation from specular components (SC)-only channel models, which are defined by the geometrical structures of the sensing targets in the environment, including time of arrival (ToA) delay, angle of departure (AoD), angle of arrival (AoA), and Doppler, among others [22]–[25]. However, an important propagation effect widely studied in channel modeling (CM) literature, while remaining largely underexplored in ISAC, is the dense multipath components (DMC) [26]–[31]. DMC refers to clutter, such as diffuse scattering and diffraction, from the background environment (and also scatterers) [26]. For example, DMC could rise from surface roughness and irregularities, building structure, or walls, etc. These propagation effects are frequency-dependent and should be modeled differently across sub-bands. Moreover, since DMC are modeled as non-resolvable multipath components, their magnitude scale with transmit power and should hence be treated as interference.

DMC is a dominant impairment in practical multi-band ISAC channels and must be explicitly captured in the system

Manuscript received XXX.

Dexin Wang, Ahmad Bazzi, and Marwa Chafii are with the Engineering Division, New York University Abu Dhabi (NYUAD), P.O. Box 129188, Abu Dhabi, UAE and NYU WIRELESS, NYU Tandon School of Engineering, Brooklyn, NY 11201, USA (email: oscarwang@nyu.edu, ahmad.bazzi@nyu.edu, marwa.chafii@nyu.edu).

Roberto Bomfin is with the Engineering Division, New York University Abu Dhabi (NYUAD), P.O. Box 129188, Abu Dhabi, UAE (email: roberto.bomfin@nyu.edu).

model to obtain meaningful sensing conclusions. In contrast to the common intuition, the reflected signal power alone is not a reliable proxy for parameter estimation performance once DMC is present: DMC, as interference, grows with the SC, and may even shadow the weak SC peaks, degrading sensing performance even at high received power. Neglecting DMC leads to systematically misleading results: from a system-level perspective, it yields over-optimistic, unrealistic predictions of sensing performance. From a signal processing perspective, it introduces non-negligible estimation bias and unexpectedly large errors, and yields erroneous internal reliability metrics for the estimated parameters.

In multi-band settings, DMC becomes even more determinant because its statistics are frequency-dependent. In our previous works [32], [33], we investigated the multi-band ISAC channel through single-band processing (i.e., without cross-band combination) and experimentally observed a key, non-intuitive behavior: lower bands, although often enjoying higher received power due to less blockage, can suffer from stronger DMC interference. So, the apparent power advantage does not necessarily translate into better sensing performance. Conversely, higher bands can exhibit sparser channels but with relatively weaker DMC contamination, so that they may achieve superior estimation due to a higher SC/DMC power ratio even at lower signal-to-noise ratio (SNR). These effects are inherently non-linear and can violate conventional single-band intuition, making a proper DMC-aware model essential for assessing the contributions of different sub-bands in multi-band ISAC performance.

B. This Work

Existing works typically fail to bridge the gap between multi-band sensing and DMC. For example, multi-band sensing works such as [17]–[20] all assumed an SC-only channel model with white Gaussian noise, while DMC-related works such as [26]–[31] are focused on CM and single-band estimation of channel parameters. Moreover, despite the DMC and multi-band sensing-related insights provided by our previous works [32], [33], they were limited to single-band estimation of SC under DMC. The theoretical framework for *combined* multi-band processing with sub-band frequency-dependent DMC remains unaddressed. Additionally, accounting for the justification of including DMC in multi-band ISAC channel models discussed in the previous subsection, all these reasons motivate the present work: to analyze the effects of DMC on combined multi-band ISAC systems and compare its estimation and detection performance with single-band processing.

Our contributions in this paper are summarized as follows. First, to understand the impact of DMC in multi-band sensing:

- We propose and analyze a novel ISAC system model for multi-band sensing involving background DMC.
- We show how the nonlinearities brought by DMC challenge conventional sensing intuitions through plots of the Cramér-Rao bound (CRB) and the modified Cassini ovals obtained from our proposed bistatic geometric gain (BGG) metric.

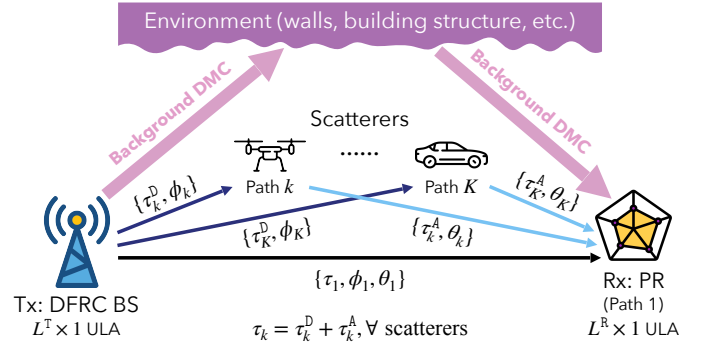


Fig. 1. Bi-static ISAC scenario with $K-1$ scatterers under background DMC interference. The geometric sensing parameters associated with each path are shown.

- We assess the sensing tradeoffs among sub-bands by analyzing CRB-based fundamental limits, showing how one sub-band may no longer dominate sensing performance under all conditions.

Then, to know how to perform multi-band sensing under DMC:

- We propose a multi-band estimator capable of resolving angular ambiguity caused by the grating lobes effect.
- We observe fundamental limits-achieving performances, with enhanced performance compared to single-band systems in terms of lower root mean squared error (RMSE) and probability of false alarm (PFA).

The remainder of this paper is organized as follows. Section II describes the multi-band system model, incorporating both the SC and DMC. Section III defines the fundamental limits and empirical metrics that help understand the non-linear impact of DMC on the estimation accuracy and detectability of the paths. Section IV details the design of our scalable multi-band estimator that resolves angular ambiguity from the grating lobes effect. Section V reports and analyzes the numerical results for the system model and the algorithm. Finally, Section VI concludes the paper and outlines directions for future research.

Notations: \otimes denotes the Kronecker product, \odot denotes the element-wise product, and $\text{toep}(\mathbf{x})$ denotes the Toeplitz matrix where the first column is \mathbf{x} and the first row is \mathbf{x}^H . Moreover, $\text{cat}_n\{\cdot\}$ denotes concatenating tensors in the set $\{\cdot\}$ in the n^{th} dimension. Also, $\{a_n\}_{n=1}^N$, which may also be written as $a_{1:N}$, denotes the set $\{a_1, a_2, \dots, a_N\}$, and $[\mathbf{a}_n]_{n=1}^N$ denotes the vertically stacked vector $[\mathbf{a}_1^T, \mathbf{a}_2^T, \dots, \mathbf{a}_N^T]^T$. Additionally, $\mathbf{0}_{\times n}$ denotes a matrix of all zeros with n columns if the number of rows can be inferred from other parts of the equation. Finally, for some matrix \mathbf{A} , $[\mathbf{A}]_{i,\cdot}$ denotes the i^{th} row, $[\mathbf{A}]_{\cdot,j}$ denotes the j^{th} column, and $[\mathbf{A}]_{i,j}$ denotes the $(i, j)^{\text{th}}$ element.

II. SYSTEM MODEL

The scenario, as shown in Fig. 1, involves a dual-function radar communication (DFRC) base station (BS) serving as the transmitter (Tx) and a passive radio (PR) as the receiver (Rx), whose Cartesian locations are assumed to be known. The Tx DFRC BS has L^T uniform linear array (ULA) antenna

elements, and the Rx PR has L^R ULA antenna elements. The PR receives the multi-band signal from the BS across M sub-bands, each with N subcarriers, and performs bi-static sensing using the downlink preamble signals from communications with user equipments (UEs) in the environment. Note that in this paper, all sub-bands are assumed to be identical in terms of the number of subcarriers, even though this may not be the case in general. The channel consists of $K - 1$ scatterers and the DMC. In addition to the scatterers, the line-of-sight (LoS) path is also estimated. In general, the LoS path serves as a reference for localizing scatterer positions when the Tx and Rx are not time-synchronized, and their respective orientations are unknown. So, accounting for both the LoS and the scatterer paths, the total number of paths is K . We assume each of our paths to be specular, meaning that the primary source of DMC is from the background environment.

In this paper, we study the typical ISAC system in which sensing is performed on the multiple-input, multiple-output (MIMO) frequency-domain channel state information (CSI). In practice, the CSI is obtained via orthogonal frequency-division multiplexing (OFDM) pilots that are designed to ensure orthogonality across Tx antennas. Following the model in [26], we express the multi-band MIMO channel transfer function (TF) $\mathbf{h} \in \mathbb{C}^{NL^T L^R M \times 1}$ by

$$\mathbf{h} = \mathbf{s} + \mathbf{d} + \mathbf{w}, \quad (1)$$

where $\mathbf{s} = [\mathbf{s}_m]_{m=1}^M$ represents the SC associated with the K paths, $\mathbf{d} \sim \mathcal{CN}(\mathbf{0}, \mathbf{R})$ represents the background DMC, and $\mathbf{w} \sim \mathcal{CN}(\mathbf{0}, \mathbf{S})$ represents the noise with covariance matrix \mathbf{S} . We use m to denote the sub-band index. We expect the radar cross section (RCS) of the scatterers, the antenna radiation patterns, and the background DMC properties to be frequency-dependent across sub-bands, while remaining constant within each sub-band. The detailed modeling approaches for each of the three parts (SC, DMC, and noise) are discussed in the following subsections.

A. The Specular Components (SC)

For a fixed environment (i.e., placement of Tx, Rx, and the scatterers) over the entire signal duration, the SC is generally considered to be time-invariant, i.e., not changing across different realizations of the channel. Hence, each $\mathbf{s}_m \in \mathbb{C}^{NL^T L^R \times 1}$ represents the specular channel TF for each sub-band with frequency f_m , which is given by

$$\mathbf{s}_m = \sum_{k=1}^K g_{k,m} \mathbf{a}_m(\tau_k, \phi_k, \theta_k), \quad (2)$$

where $\mathbf{a}_m(\tau_k, \phi_k, \theta_k)$ is the total steering vector for path k at sub-band m described by the geometric parameters, and $g_{k,m}$ is the path gain for path k at sub-band m .

1) *Geometric parameters*: The geometric parameters of the k^{th} path include the ToA delay τ_k relative to the LoS, the AoD ϕ_k relative to the Tx array broadside, and the AoA θ_k relative to the Rx array broadside. They contribute to the SC part of the channel model through the total steering vector, which can be factorized as [26]

$$\mathbf{a}_m(\tau_k, \phi_k, \theta_k) = \mathbf{a}_m^F(\tau_k) \otimes \mathbf{a}_m^T(\phi_k) \otimes \mathbf{a}_m^R(\theta_k). \quad (3)$$

The path index k is designated as follows: $k = 1$ corresponds to the LoS path, and $k = 2 \cdots K$ corresponds to the scatterers. Assuming typical far-field propagation and narrowband antenna array response [26], the factorized terms of the SC steering vector can be expressed as

$$\mathbf{a}_m^F(\tau) = [\exp(-jn\omega_{\Delta,m}\tau)]_{n=0}^{N-1}, \quad (4)$$

$$\mathbf{a}_m^T(\phi) = [\exp(-j\omega_m(d^T/c)\ell \sin \phi)]_{\ell=0}^{L^T-1}, \quad (5)$$

$$\mathbf{a}_m^R(\theta) = [\exp(-j\omega_m(d^R/c)\ell \sin \theta)]_{\ell=0}^{L^R-1}, \quad (6)$$

where $\omega_m = 2\pi f_m$, $\omega_{\Delta,m} = 2\pi f_{\Delta,m}$ is the subcarrier spacing, and d^T and d^R are the antenna spacings of the Tx and Rx ULA, respectively.

2) *Path gains*: In multi-band sensing, ideally, the same hardware is used across different sub-bands. Thus, we assume fixed-aperture antennas instead of fixed-gain ones, leading to varying antenna directivity patterns across sub-bands. Additionally, the RCSs of the scatterers are highly frequency-dependent. Accurately modeling every single detail of the path gains requires a high degree of complexity due to the large number of variables, which compromises generalizability and is not the focus of this paper. Thus, we opted for the following model, which absorbs many parameters, including $\lambda_m^2/4\pi$, the RCS of the scatterers $\sigma_{k,m}^{\text{RCS}} (\forall k > 1)$, the Tx and Rx antenna directivity patterns $u_m^T(\phi)$ and $u_m^R(\theta)$, and phase terms such as $e^{-j\omega_m \tau_k}$ into the complex path coefficient $\gamma_{k,m}$.

The gain of the LoS path ($k = 1$) is modeled by the Friis' equation

$$g_{1,m} = \gamma_{1,m} \sqrt{\frac{P^T f_{\Delta,m}}{4\pi(c\tau_1)^2}}, \quad (7)$$

where

$$|\gamma_{1,m}| = \sqrt{\frac{\lambda_m^2 u_m^T(\phi) u_m^R(\theta)}{4\pi}}, \quad (8)$$

and the complex path gain for each scatterer's SC $g_{k,m}$ ($k > 1$) is modeled by the two-way bistatic radar equation

$$g_{k,m} = \gamma_{k,m} \sqrt{\frac{P^T f_{\Delta,m}}{(4\pi)^2 (c\tau_k^D)^2 (c\tau_k^A)^2}}, \quad (9)$$

where

$$|\gamma_{k,m}| = \sqrt{\frac{\lambda_m^2 \sigma_{k,m}^{\text{RCS}} u_m^T(\phi) u_m^R(\theta)}{4\pi}}. \quad (10)$$

In the above equations (7)-(10), P^T is the fixed average transmit power spectral density across symbols, τ_k^D is the delay between the Tx and the scatterer, τ_k^A is the delay between the scatterer and the Rx, and $\gamma_{k,m}$ is the frequency-dependent complex path coefficient ($k = 1$ for the LoS path). The average transmit power per subcarrier across symbols on the m^{th} subband is thus $P^T f_{\Delta,m}$.

For the purpose of this paper, it is also sufficient to capture the typical case where the path coefficient magnitude $|\gamma_{k,m}|$ decreases with f_m . This assumption is consistent with two well-established physical trends. First, propagation losses associated with diffuse scattering, diffraction, and penetration through the scatterers generally increase at higher frequencies for most real-world scatterers with electrically rough surfaces,

as reported in the ultra-wideband (UWB) and propagation physics literature [34]–[37]. Second, for a fixed-size antenna, the electrical aperture grows with frequency, causing the radiation pattern to become more directive as f_m increases [38]. According to antenna physics and the conservation of energy, when a path is not aligned with the boresight direction, the corresponding directivity typically oscillates with frequency but has a non-increasing envelope [39]. This envelope trend contributes to a general frequency-dependent reduction in the effective gain observed by off-boresight paths.

B. The Dense Multipath Components (DMC)

Since DMC arise from small surface details such as roughness, it may suffer from randomness across channel realizations due to small-scale mobility, i.e. translation or rotation of the Tx, Rx, and background scatterers on the order of wavelengths, which causes the phases of the individual DMC in one resolvable delay/angle bin to vary randomly across an extended period of time even if the SC stays constant. From the central limit theorem, in each delay bin, the DMC is modeled as a complex Gaussian random variable due to the large number of unresolvable DMC [26]. A typical approach to modeling the background DMC is to align it with the LoS specular path [26]. DMC profiles supporting this modeling approach are observed and measured in our other experiment-based works [32], [33].

1) *Delay domain characteristics*: The power-delay profile (PDP) of the complex Gaussian process can be modeled as an exponential decay [40]:

$$P_m^{\text{DS}}(\tau, \tau_1) = \begin{cases} 0 & \tau < \tau_1, \\ \alpha |g_{1,m}|^2 / 2 & \tau = \tau_1, \\ \alpha |g_{1,m}|^2 e^{-\beta_m(\tau-\tau_1)} & \tau > \tau_1, \end{cases} \quad (11)$$

where the maximum power of the DMC is modeled as a fraction of the LoS SC power quantified by α , and β_m is the sub-band frequency-dependent decay rate. DMC PDPs that can be described by this model are measured and observed in our experiment-based work [32]. By calculating the Fourier Transform of the PDP, the frequency correlation function (FCF), we can see that the decay rate can be interpreted as the coherence bandwidth of the DMC on sub-band m , which contains the delay spread (DS) information. The finite bandwidth sampled version of the FCF is given by [26]

$$\mathbf{r}_m^{\text{F}} = \frac{\alpha |g_{1,m}|^2}{N} \left[\frac{e^{-jn\omega_{\Delta,m}\tau_1}}{\tilde{\beta}_m + \frac{j2\pi n}{N}} \right]_{n=0}^{N-1}, \quad (12)$$

where $\tilde{\beta}_m = \beta_m / (N-1)\Delta\omega_m$ is the coherence bandwidth normalized to the measurement bandwidth $(N-1)\Delta\omega_m$. In the frequency domain, the complex Gaussian process is Fourier-transformed and sampled at the subcarriers, hence becoming joint complex Gaussian random variables following the distribution $\mathcal{CN}(\mathbf{0}, \mathbf{R}_m^{\text{F}})$, where $\mathbf{R}_m^{\text{F}} \in \mathbb{C}^{N \times N}$ is obtained from the FCF and is given by

$$\mathbf{R}_m^{\text{F}} = \text{toep}(\mathbf{r}_m^{\text{F}}). \quad (13)$$

2) *Angle domain characteristics*: The power-angular profile (PAP) can be modeled as a Von-Mises distribution (VMD) [26]:

$$P_m^{\text{AS}}(\phi, \phi_1) = \frac{e^{\kappa_m \cos(\phi-\phi_1)}}{2\pi I_0(\kappa_m)}, \quad (14)$$

where κ_m is the sub-band frequency-dependent VMD parameter containing the angular spread (AS) information. Note that since we consider the maximum powers in the PDP, we do not have to scale the PAP. To account for the contribution from each incremental AoD and AoA, an integration of the profile over the AS is performed. We can write the angular covariance matrix of the DMC as

$$\mathbf{R}_m^{\text{T}} = \text{toep}(\mathbf{r}_m^{\text{T}}), \quad (15)$$

where

$$\mathbf{r}_m^{\text{T}} = \left[\int_{-\pi}^{\pi} |u_m^{\text{T}}(\phi)|^2 P_m^{\text{AS}}(\phi, \phi_1) [\mathbf{a}_m^{\text{T}}]_{\ell} d\phi \right]_{\ell=1}^{L^{\text{T}}}. \quad (16)$$

Note that \mathbf{R}_m^{R} follows a similar structure from (14) to (16) by changing T to R and ϕ to θ .

Now, based on the above definitions and assuming independence across different sub-bands, we can compactly write the DMC covariance matrix as

$$\mathbf{R} = \text{blkdiag} \{ \mathbf{R}_m \}_{m=1}^M, \quad (17)$$

where

$$\mathbf{R}_m = \mathbf{R}_m^{\text{F}} \otimes \mathbf{R}_m^{\text{T}} \otimes \mathbf{R}_m^{\text{R}} \in \mathbb{C}^{NL^{\text{T}}L^{\text{R}} \times NL^{\text{T}}L^{\text{R}}}. \quad (18)$$

Since DMC is essentially multipath interference, they should suffer from higher diffuse scattering and diffraction as sub-band frequency increases, just like the SC. In addition, we should also expect higher pathloss exponents for the DMC as frequency increases, since the propagation environment for DMC may not be free space. Hence, a practical way to model the DMC is to assume higher decay rates $\tilde{\beta}$ and VMD parameters κ for higher frequency sub-bands. This trend of increasing decay rates with frequency is also experimentally verified in our other work [32].

C. The Noise

We assume the noise is white; thus, the noise covariance matrix is modeled as

$$\mathbf{S} = \text{blkdiag} \{ \mathbf{S}_m \}_{m=1}^M = \text{blkdiag} \{ \sigma_m^2 \mathbf{I} \}_{m=1}^M, \quad (19)$$

and

$$\sigma_m^2 = \text{NF} \cdot N_0 f_{\Delta,m} \quad (20)$$

is the per-subcarrier noise variance for sub-band m , where N_0 is the white Gaussian noise power spectral density and NF is the noise figure.

In this work, our goal is to investigate the impact of DMC on multi-band sensing. Therefore, communication–sensing trade-offs in channel estimation are not incorporated into the model. We remark that when channel estimation is performed using payload data instead of pilots, the resulting estimation error is generally colored rather than white. Nevertheless, the conclusions of this study remain valid, since our model accommodates an arbitrary noise covariance matrix.

III. FUNDAMENTAL LIMITS AND EMPIRICAL METRICS

Our problem definition for this work is that given the background DMC-affected multi-band MIMO channel TF \mathbf{h} at the Rx, we should be able to jointly estimate the sensing parameters, including the number of paths K , the geometric parameters of the paths AoAs, AoDs, ToAs, and the path gains. In this paper, we assume the covariance matrices of the background DMC and white Gaussian noise are known.

The CRB-based fundamental limits and the empirical metrics of the system discussed in this section are crucial for drawing intuitive and novel insights on multi-band sensing by capturing the interplay between SC, DMC, and noise effects simultaneously. They are also helpful for designing estimation algorithms by signaling the performance bounds.

A. Cramér-Rao Bound (CRB)

Assuming independence between the background DMC and Gaussian noise, the distribution of \mathbf{h} can be modeled as

$$\mathbf{h} \sim \mathcal{CN}(\mathbf{s}, \mathbf{M}) \quad (21)$$

where

$$\mathbf{M} = \text{blkdiag}\{\mathbf{M}_m\}_{m=1}^M = \text{blkdiag}\{\mathbf{R}_m + \mathbf{S}_m\}_{m=1}^M \quad (22)$$

is known in the context of this paper. Hence, exploiting the block-diagonal structure of \mathbf{M} , following the general complex Gaussian Fisher information matrix (FIM) structure in [41], the FIM is constructed as follows

$$\mathbf{F} = \sum_{m=1}^M \mathbf{F}_m = \sum_{m=1}^M 2\Re\{\mathbf{D}_m^H \mathbf{M}_m^{-1} \mathbf{D}_m\}, \quad (23)$$

where \mathbf{D}_m is the Jacobian formed by the partial derivatives of the mean vector \mathbf{s} (the SC) with respect to the sensing parameters on each sub-band. The CRB of the i^{th} parameter can hence be obtained by $\text{CRB}_i = [\mathbf{F}^{-1}]_{i,i}$.

We now derive expressions for the Jacobian matrix \mathbf{D} of the FIM. We need

$$\mathbf{D}_m = \text{cat}_2\{\mathbf{D}_m^\tau, \mathbf{D}_m^\phi, \mathbf{D}_m^\theta, \mathbf{D}_m^{\Re g}, \mathbf{D}_m^{\Im g}\}. \quad (24)$$

First, for \mathbf{s} with respect to the geometric parameters, we have

$$\mathbf{D}_m^\tau = \text{cat}_2\left\{g_{k,m} \frac{\partial}{\partial \tau_k} \mathbf{a}_m(\tau_k, \phi_k, \theta_k)\right\}_{k=1}^K, \quad (25)$$

and \mathbf{D}_ϕ and \mathbf{D}_θ follow similar structures from (25) by changing τ to ϕ and θ . Due to the Kronecker structure, we only need to know the following:

$$\frac{\partial \mathbf{a}_m^{\mathbf{F}}}{\partial \tau_k} = \mathbf{a}_m^{\mathbf{F}} \odot [-jn\omega\Delta_m]_{n=0}^{N-1}, \quad (26)$$

$$\frac{\partial \mathbf{a}_m^{\mathbf{T}}}{\partial \phi_k} = \mathbf{a}_m^{\mathbf{T}} \odot [-j\omega_m (d^{\mathbf{T}}/c)\ell \cos \phi_k]_{\ell=0}^{L-1}, \quad (27)$$

$$\frac{\partial \mathbf{a}_m^{\mathbf{R}}}{\partial \theta_k} = \mathbf{a}_m^{\mathbf{R}} \odot [-j\omega_m (d^{\mathbf{R}}/c)\ell \cos \theta_k]_{\ell=0}^{L-1}, \quad (28)$$

Then, for \mathbf{s} with respect to the gains, we have

$$\mathbf{D}_m^{\Re g} = \text{cat}_2\left\{[\mathbf{0}_{\times(m-1)}, \mathbf{a}_m(\tau_k, \phi_k, \theta_k), \mathbf{0}_{\times(M-m)}]\right\}_{k=1}^K, \quad (29)$$

$$\mathbf{D}_m^{\Im g} = \text{cat}_2\left\{[\mathbf{0}_{\times(m-1)}, j\mathbf{a}_m(\tau_k, \phi_k, \theta_k), \mathbf{0}_{\times(M-m)}]\right\}_{k=1}^K. \quad (30)$$

Note that in this paper, although the gains $g_{k,m}$ are modeled with dependence on the bistatic delays τ_k^{D} and τ_k^{A} , our algorithm estimates the gains and delays independently. Thus, our CRB formulation also ignores the dependence of the gains on the delays.

B. The Approximate CRB

In Section IV, we propose a multi-band estimator based on CRB-weighted combining. To assess the performance of this estimator, we need to derive its CRB, which is an approximation to the exact joint CRB derived in the previous subsection. This approximate CRB also plays a crucial role in evaluating the performance loss of the proposed estimator compared to the ideal joint multi-band estimator. The approximate CRB takes the form

$$\text{CRB}_{\psi_k}^{\text{approx}} = \left(\sum_{m=1}^M \text{CRB}_{\psi_k, m}^{-1}\right)^{-1} \quad (31)$$

(see Appendix A for detailed derivations).

This approximation is equivalent to ignoring the cross terms in the FIMs $\mathbf{F}_m, \forall m$. Thus, it is obvious that if the paths are less coupled, the approximate CRB better approximates the exact CRB. Also, since all CRB terms are positive, we can notice that

$$\sum_{m'=1}^M \text{CRB}_{\psi_k, m'}^{-1} \geq \text{CRB}_{\psi_k, m}^{-1}, \forall m. \quad (32)$$

Inverting both sides and using the definition in (31), we obtain

$$\text{CRB}_{\psi_k}^{\text{approx}} \leq \text{CRB}_{\psi_k, m}, \forall m, \quad (33)$$

suggesting that the approximate multi-band CRB discussed in this subsection serves as a lower bound to the exact single-band CRBs for any sub-band.

C. Estimation Signal-to-Noise Ratio (ESNR)

The estimation signal-to-noise ratio (ESNR) can be thought of as a measure of the certainty of an estimated path. One crucial issue that needs to be addressed when estimating the SC parameters is how the algorithm should determine whether a peak is SC or part of the DMC profile. Another similar issue is whether the algorithm can trust estimates from a particular sub-band when combining across sub-bands. Both of these issues could be addressed by using ESNR.

For a true path with gain $g_{k,m}$, the ESNR $\mu_{k,m}$ is defined as

$$\mu_{k,m} = \frac{|g_{k,m}|^2}{\text{CRB}_{|g_{k,m}|}}, \quad (34)$$

where $\text{CRB}_{|g_{k,m}|}$ can be obtained from $\text{CRB}_{\Re g_{k,m}}$ and $\text{CRB}_{\Im g_{k,m}}$ through a Jacobian coordinate transformation on the FIM. We can see that if the ESNR is low, the variance of our estimate will be so large compared to the true value that it is no longer informative for estimation. In our work, the ESNR plays an instrumental role in multi-band sensing, serving as the threshold for deciding which sub-band estimates to combine.

D. Bistatic Geometric Gain (BGG)

To investigate the combined effect of both DMC and noise on the SC, it is meaningful to examine a metric that captures their joint spatial interplay while preserving the geometric intuition commonly used in ISAC and radar analysis. In classical bistatic radar formulations, performance metrics such as received power or detection SNR depend on the product of Tx-scatterer and scatterer-Rx distances, naturally giving rise to *Cassini ovals* as contours of equal sensing performance [42], [43]. These ovals provide an intuitive visualization of geometry-induced performance variations under free-space and noise-limited assumptions.

In our more realistic ISAC case, however, sensing performance is not governed solely by the SC and thermal noise. The presence of DMC introduces a spatially structured interference term whose power depends on both delay- and angular-domain profiles, fundamentally altering the spatial behavior of estimation performance. Interpretations from classical Cassini ovals, therefore, become insufficient, as they neglect the frequency-dependent and geometry-dependent impact of DMC. This consequence motivates the introduction of a metric that explicitly accounts for the combined contributions of SC, DMC, and noise on sensing performance.

To this end, we define the BGG metric for the m^{th} sub-band as

$$\Gamma_m(\mathbf{p}) = \frac{G_m^{\text{SC}}(\mathbf{p})}{G_m^{\text{DMC}}(\mathbf{p}) + \sigma_m^2}, \quad (35)$$

where \mathbf{p} denotes the Cartesian coordinates of a 2D location. The numerator

$$G_m^{\text{SC}}(\mathbf{p}) = \frac{P^{\text{T}} f_{\Delta, m}}{(4\pi)^2 (c\tau^{\text{D}}(\mathbf{p}))^2 (c\tau^{\text{A}}(\mathbf{p}))^2} \quad (36)$$

corresponds to the geometry-induced power of the SC, which depends on the product of bistatic path lengths. The denominator

$$G_m^{\text{DMC}}(\mathbf{p}) = \frac{P_m^{\text{DS}}(\tau(\mathbf{p}), \tau_1) \cdot P_m^{\text{AS}}(\phi(\mathbf{p}), \phi_1) \cdot P_m^{\text{AS}}(\theta(\mathbf{p}), \theta_1)}{|\gamma_{1, m}|^2}, \quad (37)$$

together with the sub-band noise variance σ_m^2 , captures the spatially varying, geometry-induced contribution of DMC.

By construction, the BGG metric isolates the geometry-dependent interaction between SC, DMC, and noise by factoring out path-dependent coefficients $\gamma_{k, m}$ and the impact of the sub-band dependent antenna directivity patterns $u_m^{\text{T}}(\phi)$ and $u_m^{\text{R}}(\theta)$ on the angular distribution of DMC. Its level sets can therefore be interpreted as *modified Cassini ovals*, where equal values of Γ_m correspond to locations exhibiting comparable signal-to-interference-and-noise ratio (SINR)-like conditions for estimation. When $G_m^{\text{DMC}}(\mathbf{p}) = 0$, i.e., in the absence of DMC interference, the modified Cassini ovals naturally coincide with the conventional Cassini ovals. As such, the BGG metric provides a physically meaningful and interpretable proxy for sensing performance in DMC-affected multi-band ISAC scenarios.

E. Probabilities of Detection and False Alarm

One of the main advantages of our proposed multi-band estimation algorithm outlined in Section IV is its ability

to resolve the angular ambiguities caused by the grating lobes effect. To quantitatively characterize this behavior, we introduce the probability of detection (PD) and PFA metrics and investigate the resulting PD-PFA curves.

Let \mathcal{H}_K denote the hypothesis that the environment contains K paths (including the LoS path), and let $\hat{\mathcal{X}} \subseteq \mathbb{R}^3$ denote the set containing the geometric parameters of all estimated paths returned by the algorithm, where each element is $\hat{\mathbf{x}} = [\hat{\tau}, \hat{\phi}, \hat{\theta}]$. For the k^{th} true path with geometric parameters $\mathbf{x}_k = [\tau_k, \phi_k, \theta_k]$, we define its region of detection as

$$\mathcal{D}_k = \{\hat{\mathbf{x}} \in \mathbb{R}^3 : \|\mathcal{T}(\hat{\mathbf{x}}) - \mathcal{T}(\mathbf{x}_k)\|_2 \leq R\}, \quad (38)$$

where R is the detection radius and $\mathcal{T}(\cdot)$ is a resolution-aware normalization mapping explained in detail in the later paragraphs. We then define the PD and PFA as

$$\text{PD} = \Pr\left(\forall k \in \{1, 2, \dots, K\}, \left|\hat{\mathcal{X}} \cap \mathcal{D}_k\right| > 0 \mid \mathcal{H}_K\right), \quad (39)$$

$$\text{PFA} = \Pr\left(\exists \hat{\mathbf{x}} \in \hat{\mathcal{X}} \text{ s.t. } \hat{\mathbf{x}} \notin \bigcup_{k=1}^K \mathcal{D}_k \mid \mathcal{H}_K\right). \quad (40)$$

The normalization mapping $\mathcal{T} : \mathbb{R} \times (-90^\circ, 90^\circ)^2 \rightarrow \mathbb{R} \times \left(-\frac{2}{L^{\text{T}}}, \frac{2}{L^{\text{T}}}\right) \times \left(-\frac{2}{L^{\text{R}}}, \frac{2}{L^{\text{R}}}\right)$ is defined as

$$\mathcal{T}([\tau, \phi, \theta]) = \left[N f_{\Delta, 0} \tau, \frac{2 \sin \phi}{L^{\text{T}}}, \frac{2 \sin \theta}{L^{\text{R}}} \right]. \quad (41)$$

It is designed to compare delay/angle values in a dimensionless, resolution-aware coordinate system that matches the natural phase variables of the OFDM-MIMO steering vectors.

Specifically, we acknowledge a well-known relation that the delay resolution scales with $1/(N f_{\Delta})$, where $N f_{\Delta}$ is the occupied bandwidth. Since the goal is to normalize the delays and angles for comparison across sub-bands, we choose a reference subcarrier spacing $f_{\Delta, 0}$ to be $f_{\Delta, 1}$, the subcarrier spacing of the lowest sub-band. Dividing the delay value τ by the corresponding resolution yields the normalized delay coordinate $N f_{\Delta, 0} \tau$. To extend this approach to the angle domain, we observe a structural similarity between the frequency and space-domain steering vectors. While delay induces a linear phase progression across subcarriers through the term $e^{-j2\pi n f_{\Delta} \tau}$, angles induce a linear phase progression across ULA array elements through the spatial frequency term $e^{-j2\pi (d/\lambda) \ell \sin(\cdot)}$. Consequently, angular resolution scales with $1/(L(d/\lambda))$ if the angle is transformed by $\sin(\cdot)$. By selecting a reference wavelength λ_0 such that $\lambda_0 = 2d$, the normalized angular coordinates $2 \sin \phi / L^{\text{T}}$ and $2 \sin \theta / L^{\text{R}}$ are produced. As a result, Euclidean distances after \mathcal{T} reflect discrepancies in approximately comparable resolution units across delay and angle, preventing the matching metric from being dominated by heterogeneous physical units and better aligning the association cost with the steering-vector sensitivity.

IV. PROPOSED MULTI-BAND ESTIMATION ALGORITHM

In this section, we propose a scalable multi-band estimator based on combining single-band estimators. This is a practical solution for tractability because we focus on multi-band processing, while the full multi-band estimation problem is very

complex. For the single-band estimators, we choose the well-known state-of-the-art estimation algorithm proposed in [40], based on the iterative Levenberg-Marquardt (LM) approach. This estimator is known to achieve the CRB.

A. Overview of the Algorithm

To easily accommodate multi-band operation, we wish to perform a linear combination of the estimated geometric parameter values (ToAs, AoAs, and AoDs) from the single-band estimators. When the estimators for every sub-band are efficient (i.e., they approach their own CRB), we can obtain the minimal variance linear unbiased estimator by designing weights (for any sub-band m where some geometric parameter ψ_k is estimated) as [41]

$$w_{\hat{\psi}_{k,m}} = \frac{\text{CRB}_{\hat{\psi}_{k,m}}^{-1}}{\sum_{\forall m \text{ detected}} \text{CRB}_{\hat{\psi}_{k,m}}^{-1}} \quad (42)$$

(see Appendix A for detailed derivations).

Since our antenna spacings d^T and d^R are fixed while multiple frequencies are used, we could observe *grating lobes* (i.e. spatial aliasing in angular domains) for certain AoAs or AoDs when $d > \lambda_m/2$. Take AoD as an example. For the i^{th} real angle $\hat{\phi}_i$ estimated from a single-band estimator with wavelength λ , aliased angles $\hat{\phi}_i^r$ should appear at [44]

$$\hat{\phi}_i^r = \sin^{-1}(\sin \hat{\phi}_i + r\lambda/d^T), \quad (43)$$

where $r \in \{\pm 1, \pm 2, \dots\}$ can be any value that makes $\sin^{-1}(\cdot)$ take values in $[-1, 1]$. We can also denote $\hat{\phi}_i$ by $\hat{\phi}_i^0$. Hence, for each estimated real path, we consider all its aliased versions as a *path group*. Across the three records, the same path group is indexed by the same index p . Also, note that a perfect scheme for resolving ambiguity is beyond the scope of this paper.

The algorithm iterates over every sub-band m , and it dynamically keeps and updates, per valid iteration, three data containers of all estimated path groups:

- **Estimates of Unambiguous Groups \mathcal{E}_U** : the latest weighted combined estimates of the unambiguous path groups ($p \in \mathcal{U}_m$). At each sub-band iteration m , the term corresponding to each geometric parameter is a scalar. For example, this record can contain the latest weighted combined AoD estimate for path 2, denoted by $\hat{\phi}_2$.
- **Estimates of Ambiguous Groups \mathcal{E}_A** : the latest estimates of the ambiguous path groups. At each sub-band iteration m , the term corresponding to each geometric parameter is a set. For example, this record can contain the latest AoD estimate for the ambiguous path group 3, denoted by $\hat{\phi}_3 = \{\hat{\phi}_3^r\}_{r \in \{0, \pm 1, \pm 2, \dots\}}$.
- **Record of Unambiguous Groups \mathcal{R}_U** : the record for the estimates per iteration m of the unambiguous path groups ($p \in \mathcal{U}_m$). At each sub-band iteration m , the term corresponding to each geometric parameter is a $1 \times m$ vector. For example, this record can contain a vector with all past AoD estimates for path 2, denoted by $\hat{\phi}_2 = [\hat{\phi}_2^{(1)}, \hat{\phi}_2^{(2)}, \dots, \hat{\phi}_2^{(m)}]$.

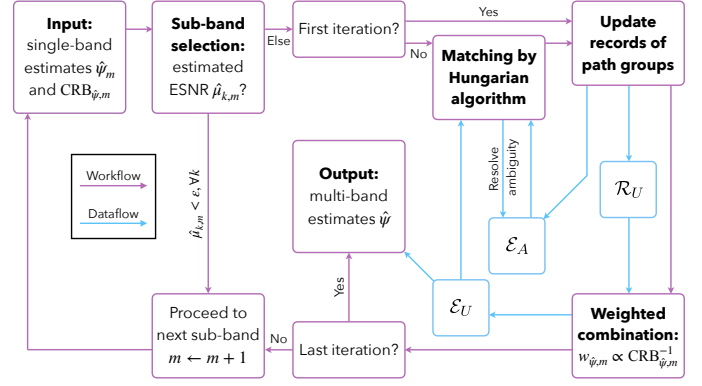


Fig. 2. Flowchart of the algorithm. Each subsection that discusses the algorithm from IV-B to IV-E corresponds to a box with bolded text.

A summary of the algorithm is provided in the flowchart of Fig. 2, where $\hat{\psi}$ refers to the estimate for any geometric parameter ψ (including ToA τ , AoD ϕ , or AoA θ). Some details of the algorithm are discussed in the following subsections.

B. Sub-Band Selection

Since ESNR is a measure of how certain we can trust a path seen by a given sub-band, we use it for sub-band selection. In the algorithm, the estimated values are used instead of the true values to form the estimated ESNR

$$\hat{\mu}_{k,m} = \frac{|\hat{g}_{k,m}|^2}{\text{CRB}_{|\hat{g}_{k,m}|}}. \quad (44)$$

If $\hat{\mu}_{k,m} < \epsilon_{\text{ESNR}}, \forall k$, where ϵ_{ESNR} is the predefined ESNR threshold, the sub-band is uncertain and should be dropped for combining. This step is added after we observed that in low SNR regions, where the CRB is not achieved, combining harms estimation accuracy, as it may make the multi-band estimator even less accurate than the better single-band estimator.

C. Matching by Hungarian Algorithm

To simultaneously associate estimates across sub-bands and eliminate the aliased estimated angles, we use the Hungarian matching algorithm. In each valid iteration on sub-band m , we first perform the matching between the overall latest estimated groups (the terms in \mathcal{E}_U and \mathcal{E}_A , whose index is p) and the newly estimated path groups from the single-band estimator of this sub-band (whose index is i). The inter-group matching cost $[\mathcal{C}_m]_{p,i}$, which is the $(p, i)^{\text{th}}$ term of the Hungarian matching cost matrix \mathcal{C}_m , is computed based the minimal ℓ_2 -distance between all ambiguity versions of the transformed geometric parameters of both groups as follows

$$[\mathcal{C}_m]_{p,i} = \min_{r_{1:4}} \|\mathcal{T}(\hat{\mathbf{x}}_p^{r_{1:4}}) - \mathcal{T}(\hat{\mathbf{x}}_i^{r_{1:4}})\|_2, \quad (45)$$

$$r_{1:4}^* = \arg \min_{r_{1:4}} \|\mathcal{T}(\hat{\mathbf{x}}_p^{r_{1:4}}) - \mathcal{T}(\hat{\mathbf{x}}_i^{r_{1:4}})\|_2, \quad (46)$$

where $\hat{\mathbf{x}}_p^{r_{1:4}}$ denotes $[\hat{\tau}_p, \hat{\phi}_p^{r_1}, \hat{\theta}_p^{r_2}]$, $\hat{\mathbf{x}}_i^{r_{1:4}}$ denotes $[\hat{\tau}_i, \hat{\phi}_i^{r_3}, \hat{\theta}_i^{r_4}]$, $r_{1:4}^*$ stores the optimal ambiguity version indices for computing this cost, and \mathcal{T} denotes the same resolution-aware normalization mapping defined in (41). Note that the Hungarian

matching algorithm can optionally take a maximum cost input, C_{\max} , to prevent matching two path groups that are far apart. We also compute the prominence $[\mathbf{P}_m]_{p,i}$ for the matching cost of each matched pair of groups (p, i) , which is defined as

$$[\mathbf{P}_m]_{p,i} = \min_{r_1:4 \neq r_1:4} \|\mathcal{T}(\hat{\mathbf{x}}_p^{r_1:r_2}) - \mathcal{T}(\hat{\mathbf{x}}_i^{r_3:r_4})\|_2 - [\mathbf{C}_m]_{p,i}. \quad (47)$$

The ambiguity of an ambiguous p -indexed overall latest group is resolved if both of the following conditions hold:

- A matching exists between it and some i -indexed newly estimated path group after running the Hungarian matching algorithm,
- The matched pair of path groups (p, i) satisfies the minimum prominence condition $[\mathbf{P}_m]_{p,i} > \varepsilon_{\text{prom}}$, where $\varepsilon_{\text{prom}}$ is the predefined prominence threshold.

We also know which aliased version should now be regarded as the true estimate of this previously ambiguous group. For example, we can now deduce that $\hat{\phi}_p^{(m_a)} = \hat{\phi}_p^{r_1}$ and $\hat{\phi}_i^{(m)} = \hat{\phi}_i^{r_3}$, where m_a is the iteration index of the sub-band where the ambiguity of the group is first observed.

D. Update Records of Path Groups

If some i -indexed newly estimated path groups are not matched to any path groups in \mathcal{E}_U or \mathcal{E}_A , we call them *new path groups* and assign to them new p -indices. The ambiguous new path groups are directly appended to the end of \mathcal{E}_A , and the unambiguous new path groups are used to update \mathcal{R}_U before generation of the latest \mathcal{E}_U through weighted combination. We denote \mathcal{U}_m as the set of new p 's which represent unambiguous path groups after these steps, whose number of elements is used to update \hat{K} , the estimated number of paths.

Now, we discuss how to update \mathcal{R}_U by taking AoD as an example. For each $p \in \mathcal{U}_m$, we consider updating as follows the row vectors for both the parameter estimates $\hat{\phi}_p$ and the corresponding (unnormalized) weight estimates $\mathbf{c}_p^{\hat{\phi}}$:

$$[\hat{\phi}_p]_m = \begin{cases} \hat{\phi}_i & \text{if } p \text{ is matched to or converted from an } i, \\ 0 & \text{otherwise,} \end{cases} \quad (48)$$

$$[\hat{\phi}_p]_{1:m-1} = \begin{cases} \mathbf{0}_{1 \times m-1} & \text{if } p \text{ is converted from an } i, \\ [\mathbf{0}, \hat{\phi}_p^{(m_a)}, \mathbf{0}] & \text{if } p \text{ was ambiguous at } m_a, \\ \text{inherited} & \text{otherwise.} \end{cases} \quad (49)$$

The schemes for $\mathbf{c}_p^{\hat{\phi}}$ are similar, where only replacing $\hat{\phi}_i$ and $\hat{\phi}_p$ by $\text{CRB}_{\hat{\phi}_i}^{-1}$ and $\text{CRB}_{\hat{\phi}_p}^{-1}$ are needed. Additionally, similar updating schemes are applied to the other sensing parameters (except for g , for which we do not calculate the CRB-based weights vector).

E. Weighted Combination

Using the data in \mathcal{R}_U , we then update \mathcal{E}_U for all $p \in \mathcal{U}_m$ by weighted combination across all previous sub-bands through

$$\hat{\phi}_p = \frac{\hat{\phi}_p(\mathbf{c}_p^{\hat{\phi}})^T}{\hat{\phi}_p^T \mathbf{1}_{m \times 1}}, \quad (50)$$

TABLE I
NUMERICAL PARAMETERS FOR FIGS. 5 TO 9

System Parameters			
M	2	N	128
L^T	2	L^R	2
d^T	0.02 m	d^R	0.02 m
f_m	{8.75, 21.7} GHz	$f_{\Delta,m}$	{1000, 1000} kHz
$\tilde{\beta}_m$	{0.5, 1.5}	κ_m	DMC angular spread not modeled: $\mathbf{R}_m^T = \mathbf{R}_m^R = \mathbf{I}$
N_0	-174 dBm/Hz	NF	7 dB
R	0.5		
Sensing Parameters			
K	2	τ_k	{30, 32.55} ns
ϕ_k	{0, 16.72}°	θ_k	{0, 30.96}°
$\Re\gamma_{k,m}$	{0.0071, 0.0013} ($m=1$) {0.0029, 0.0005} ($m=2$)	$\Im\gamma_{k,m}$	{0.0000, -0.0095} ($m=1$) {0.0000, -0.0038} ($m=2$)
Algorithm Parameters			
$\varepsilon_{\text{ESNR}}$	6 dB	$\varepsilon_{\text{prom}}$	0.2
N_{MC}	1024	C_{\max}	0.75

and the combination schemes of $\hat{\tau}_p, \hat{\theta}_p$ follow similar forms. If $p \notin \mathcal{U}_m$, we only store them in \mathcal{E}_A for later matching, as we currently do not know which aliased version gives the real estimate.

It is evident that even after we have proceeded to the last sub-band M , there may still be some remaining ambiguous path groups in \mathcal{E}_A . At this stage, we have no choice but to ignore them. So, for every $p \in \mathcal{U}_M$, we now have the final combined estimates of the geometric parameters from \mathcal{E}_U . For the gain parameters, we report the corresponding $\hat{g}_{p,m}$'s using the \mathcal{R}_U record. Finally, we re-index the p -indices by k and pass them to the algorithm's output. The final estimated number of paths, \hat{K} , is hence given by $\hat{K} = |\mathcal{U}_M|$.

V. NUMERICAL RESULTS

We primarily aim to illustrate the expected tradeoff among the three components of the channel as we incorporate multi-band. As frequency increases, we expect lower SC power but also less DMC spreads, implying higher decay rates (and also VMD parameters, though not modeled in the simulation in this paper for tractability), leading to more concentrated DMC power to the LoS delay (and angle). For Figs. 5 to 9, a table of numerical parameters used is given in Table I, where N_{MC} is the number of Monte-Carlo simulations.

Note that the angular covariance matrices of the DMC \mathbf{R}_m^T and \mathbf{R}_m^R are modeled as \mathbf{I} in Figs. 5 to 9. This is because exact modeling of these matrices would require knowledge of the system-specific frequency-dependent antenna patterns, which is more suitable in works involving experimentation [32], [33], and this is planned for future work. Thus, we use the typical assumption of white DMC in space, without any specific antenna patterns, which is more tractable and sufficient for deriving the most important insights of the paper.

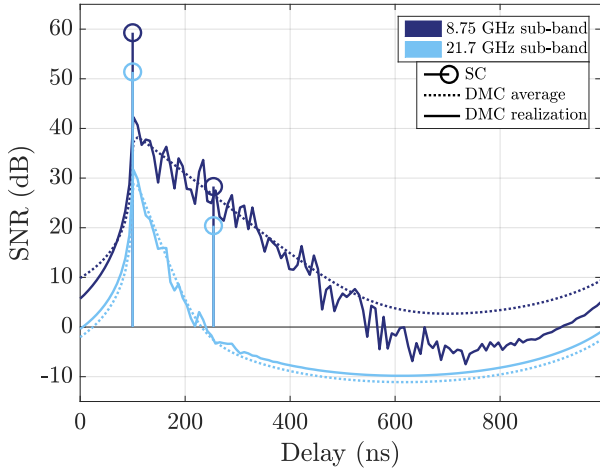


Fig. 3. The PDP of the DMC for an 8.75 GHz sub-band with a decay rate of $\tilde{\beta} = 0.5$ and a 21.7 GHz sub-band with a decay rate of $\tilde{\beta} = 1.5$ at $P^T = -40$ dBm/Hz and $\alpha = -20$ dB.

A. System Model Analysis

In this analysis, we provide a few intuitive examples of how the DMC-like clutter affects the SC estimation in multi-band ISAC. The goal of these results is to illustrate how the DMC might affect different sub-bands differently, which should be taken into account in multi-band ISAC.

1) *Channel PDP visualization*: Fig. 3 shows the DMC and SC altogether in the channel PDP when $P^T = -40$ dBm/Hz and $\alpha = -20$ dB, which provides a visual representation on how the DMC is impairing the SC estimation. We observe that DMC acts as multipath interference on the SC and scales together with the SC. As expected from the $\alpha = -20$ dB, the peak SNR of the DMC PDP sits at 20 dB below the SNR of the LoS SC. Thus, some SC, such as the reflection path for the 8.75 GHz sub-band in the figure, may be shadowed under the DMC profile. Also, due to the randomness of the DMC profile, it may be hard to distinguish SC from DMC in a finite bandwidth PDPs. Finally, it is evident in this figure that although higher sub-bands suffer from lower SC powers (e.g., for the bistatic path sitting at a delay of 254.01 ns, its SNR on the 21.7 GHz sub-band is 7.89 dB lower than that on the 8.75 GHz sub-band), they are also blessed by the faster DMC decay rates, which gives them lower interference.

In summary, this figure illustrates the complex interaction between SC and DMC profiles, where SC with less power may be more distinguishable when DMC interference is not dominant. Thus, this example highlights the importance of a complete analysis involving SC and DMC for ISAC systems.

2) *Modified Cassini ovals of BGG*: In the following results depicted in Fig. 4, we aim at incorporating the DMC interference in a modified Cassini ovals chart, by plotting the BGG contour when $P^T = -50$ dBm/Hz and $\alpha = -5$ dB. This deviation from the conventional ovals occurs when the sub-band DMC has a high κ_m , indicating that the angles are less spread. This observation may be counterintuitive in the context of traditional channel models, as it means that lower sub-bands, due to their DMC PAP being more spread out, may

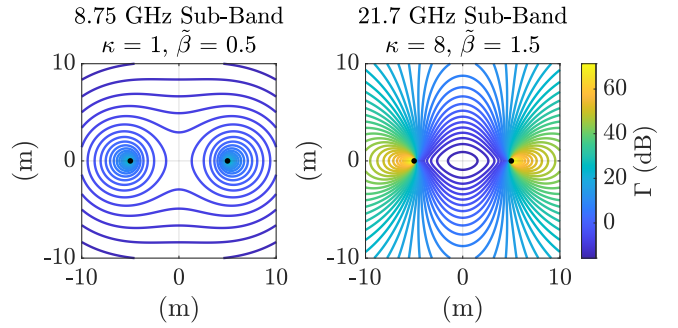


Fig. 4. The modified Cassini ovals from the BGG contours for two different sub-bands with different decay rates and VMD parameters at $P^T = -50$ dBm/Hz and $\alpha = -5$ dB.

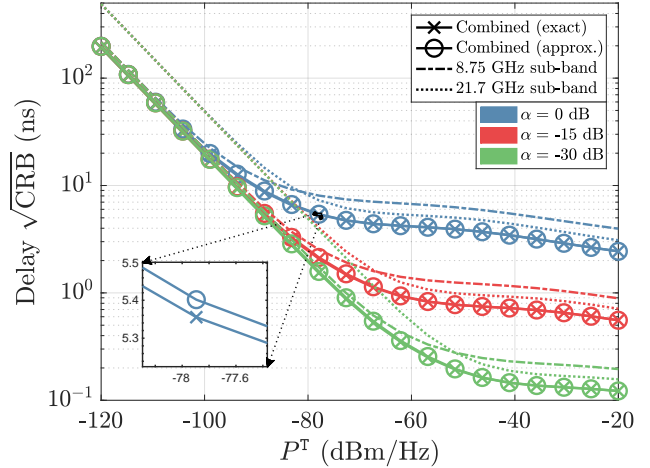


Fig. 5. The delay $\sqrt{\text{CRB}}$ vs. P^T for individual sub-bands and the combined multi-band (both approximate and exact for the latter case). The angular spread of DMC is not modeled here, i.e. $\mathbf{R}_m^T = \mathbf{R}_m^R = \mathbf{I}$.

lose the coverage advantage typically discussed in multi-band sensing compared to higher sub-bands. This observation also suggests that in some cases (usually at higher sub-bands), the existence of more concentrated DMC interference to the LoS means the BGG improves as the scatterer moves away from the Tx or Rx.

In summary, these results reveal a significant feature of multi-band ISAC systems operating in complex environments with DMC-like clutter, where the angular DMC profile may yield an unbalanced interference pattern. This phenomenon is particularly prominent in a multi-band due to a frequency-dependent DMC pattern, enabling a new degree of freedom for resource optimization.

B. Fundamental Limits Analysis

In the following, we assess the CRB derived in Section III in a single-band and multi-band setting. The goal of this analysis is to theoretically understand how the SC power and DMC clutter affect each sub-band separately, and how multi-band processing can improve the performance.

1) *CRB analysis*: Fig. 5 shows the CRB of τ_2 , the ToA of the scatterer in a two-path system. Firstly, we observe that

the approximate CRB of the proposed multi-band estimator closely follows the exact multi-band CRB curve, indicating that our proposed estimator is a simple yet effective algorithm for exploiting multi-band gains. For example, for the curve with $\alpha = 0$ dB, at an exact multi-band delay $\sqrt{\text{CRB}}$ of 5.36 ns, the difference between the approximate and the exact $\sqrt{\text{CRB}}$ values is only 0.046 ns. Next, by inspecting individual curves, we observe that in both single-band and multi-band systems with background DMC, the CRB has a noise-dominated region (at lower SNR) and a DMC-dominated region (at higher SNR). The noise-dominated region is defined as the region where the $\sqrt{\text{CRB}}$ decreases linearly on a logarithmic scale. While in the DMC-dominated region, P^T exhibits less and less effectiveness in decreasing the CRB, gradually making the CRB approach a floor. The reason behind this phenomenon is that the DMC magnitude grows with P^T . We also observe that lower α pushes the lower SNR bound of the DMC-dominated region higher and the CRB-floor in the DMC-dominated region lower, resulting in consistent drops in the logarithmic scale. For example, each 15 dB drop in α results in a decline in the delay $\sqrt{\text{CRB}}$ of about 0.65 decades.

Moreover, we observe from Fig. 5 that the two sub-bands' performances "switch" between the two SNR regions dominated by different channel effects: in the DMC dominated region, the 8.75 GHz sub-band has a higher CRB, while in the noise-dominated region, the 21.7 GHz one has a higher CRB. This behavior is because in the predominant case, we model lower path gains at higher frequencies, i.e. $|\gamma_{k,2}| > |\gamma_{k,1}|$, and at the same time, we observe more concentrated DMC profiles at higher sub-bands, with higher decay rates and sharper angular spread. Hence, the tradeoff between SC power and DMC interference power is observed. While "switching" is not guaranteed in all cases, the sole existence of such a switching phenomenon implies that one sub-band no longer dominates the estimation accuracy under all SNR conditions, further encouraging the use of multi-band sensing. We also observe that the combined multi-band system performs better than any of the constituent sub-bands at all transmit powers. In the DMC-dominated region, the improvements on the logarithmic scale are consistent at about 0.21 and 0.10 decades for the 8.75 and 21.7 GHz sub-bands, respectively, across varying α levels.

2) *ESNR analysis*: Fig. 6, as compared to Fig. 5, shows a similar trend of having a DMC-dominated region vs. a noise-dominated region but with the true ESNR of the path associated with the scatterer at a particular sub-band in a two-path system. However, in this figure, we fix the P^T while varying α . At lower α , the floor shows the Gaussian noise dominated region, since the CRB is not affected by changing α but by changing P^T ; and at higher α , the slope shows the DMC dominated region, since the CRB is not affected by changing P^T but by changing α . As explained before in the definition of the ESNR metric, when ESNR falls below a certain threshold, the CRB value associated with that path is not meaningful, as we no longer trust that estimate. It is hence dropped when the algorithm identifies reliable paths in the single-band LM estimator and the sub-band selection scheme of the multi-band weighted fusion.

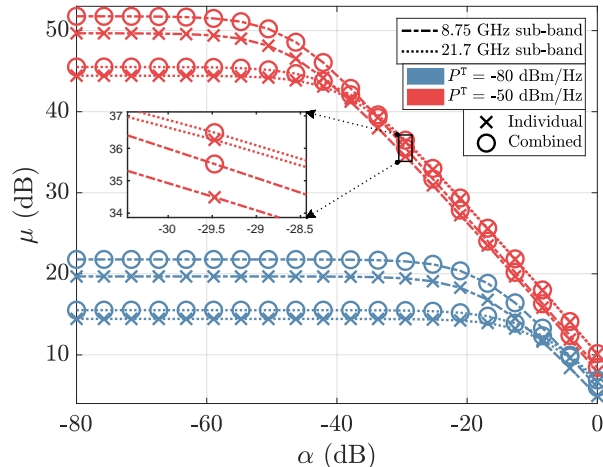


Fig. 6. The ESNR vs. α for individual sub-bands and the combined multi-band. The angular spread of DMC is not modeled here, i.e. $\mathbf{R}_m^T = \mathbf{R}_m^R = \mathbf{I}$.

We also observe from Fig. 6 that in the combined case, the two sub-bands are always helping each other, producing higher individual estimation SNRs than separate processing. This improvement is universal across sub-bands, and is not related to which sub-band has a higher ESNR or CRB. For example, at $P^T = -50$ dBm/Hz and $\alpha = -29.47$ dB, the ESNR of the 8.75 GHz sub-band is improved by 1.03 dB, and that of the 21.7 GHz sub-band is enhanced by about 0.22 dB. At $P^T = -50$ dBm/Hz and $\alpha = -67.37$ dB, the improvements increase to 2.10 and 1.08 dB, respectively, for the lower and higher sub-bands.

In summary, the above results revealed that performance in each sub-band depends on the Tx power (or LoS SNR) region. This happens because each frequency-dependent DMC yields different noise or DMC-dominated regions. This brings critical insights: (i) there is no universally best sub-band across all SNRs, (ii) multi-band processing improves the overall performance. Lastly, the CRB analysis demonstrates that the approximate CRB of our estimator based on a combination of single-band estimates is very close to the exact CRB, indicating that the proposed estimator is nearly optimal.

C. Simulation Results

In this subsection, we aim at assessing the proposed multi-band estimation described in Section IV against the CRB. In particular, we show that the relatively low-complexity strategy of combining individual single-band estimates is near-optimal, corroborating the results of Fig. 5 where the approximate CRB of the test case has practically negligible loss in relation to the exact one.

1) *RMSE performance*: Fig. 7 illustrates the estimation error in ToA when employing the proposed estimation algorithm at $\alpha = -30$ dB. First, we can see that both the multi-band estimator and the single-band estimator on the 8.75 GHz sub-band achieve the CRB at $P^T = -61.58$ dBm/Hz, while the single-band estimator on the 21.7 GHz sub-band achieves the CRB at $P^T = -58.95$ dBm/Hz. For the combined multi-band case, we compare against the exact CRB rather than

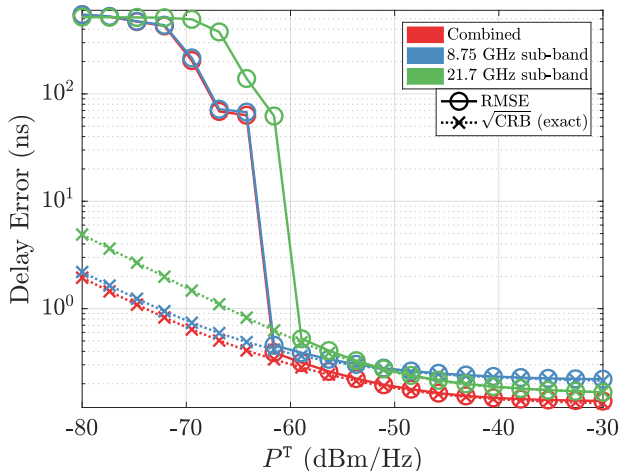


Fig. 7. Numerical delay RMSE and $\sqrt{\text{CRB}}$ vs. P^T at $\alpha = -30$ dB. The angular spread of DMC is not modeled here, i.e. $\mathbf{R}_m^T = \mathbf{R}_m^R = \mathbf{I}$.

the approximate one. Note that since the simulation is run for a discrete set of P^T values, the exact point of achieving the CRB cannot be directly inferred from the plot.

Next, the gain in RMSE performance of the combined multi-band estimator is more significant in the CRB-achieving region as compared to the single-band ones. For example, at $P^T = -30$ dBm/Hz, the delay RMSE of the combined multi-band estimator is 0.14 ns, while those for the 8.75 GHz and 21.7 GHz single-band estimators are 0.22 ns and 0.17 ns, respectively. These improvements in delay RMSE translate into reductions of 37.41% and 17.04% for the 8.75 GHz and 21.7 GHz single-band estimators, respectively. Furthermore, as predicted by the observations from Fig. 5, the gain in estimation error is especially more prominent in the “switching” region.

Finally, we can see that the ESNR-based sub-band selection scheme is especially effective in lower-SNR regimes when the estimates are not reliable (not achieving the CRB): the RMSE curve for the combined multi-band in this regime mainly follows the sub-band with the lower RMSE, with only minor improvements.

Fig. 8 illustrates the estimation error in AoD when employing the proposed estimation algorithm at $\alpha = -30$ dB. The abnormal behavior of the 21.7 GHz sub-band, where its RMSE being capped at around 12° for $P^T = -80$ to -69.47 dBm/Hz and falling below the CRB for $P^T = -80$ to -77.37 dBm/Hz, is probably due to the existence of a false ambiguity-induced peak near the true AoD. Apart from this, the AoD RMSE performance follows similar trends as compared to Fig. 7: In the high P^T region above $P^T = -53.68$ dBm/Hz, all three estimators achieves the CRB, with our combined multi-band estimator shows a gain in RMSE performance compared to the constituent sub-bands; where as in the low P^T region, the RMSE of the combined multi-band estimator generally follows the performance of the better constituent sub-band, with minor improvements. For example, at $P^T = -40.53$ dBm/Hz, the AoD RMSE for the combined multi-band estimator is 1.11° , while that for the constituent 8.75 and 21.7 GHz sub-bands

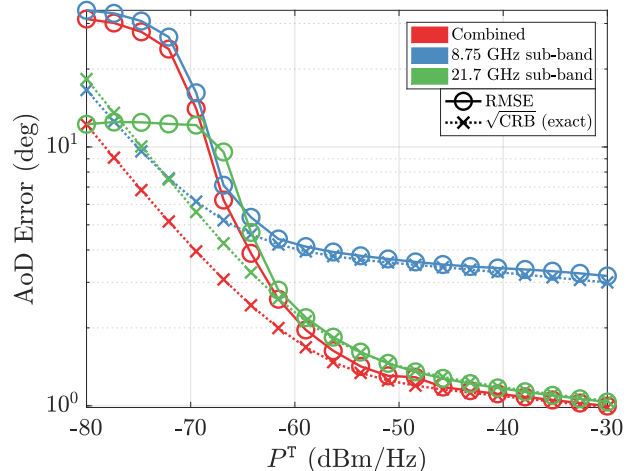


Fig. 8. Numerical AoD RMSE and $\sqrt{\text{CRB}}$ vs. P^T at $\alpha = -30$ dB. The angular spread of DMC is not modeled here, i.e. $\mathbf{R}_m^T = \mathbf{R}_m^R = \mathbf{I}$.

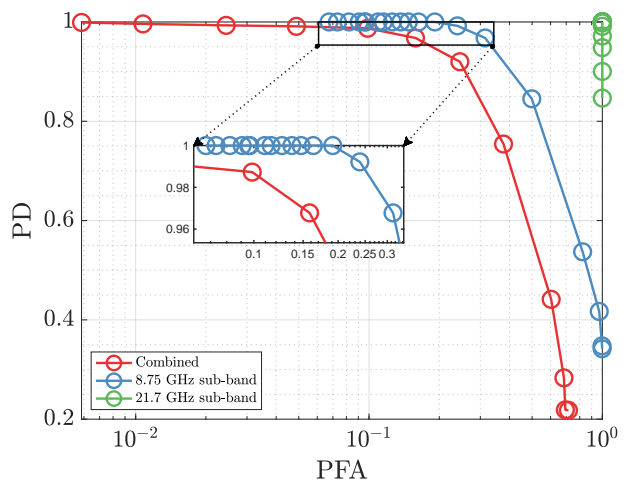


Fig. 9. PD vs. PFA at $\alpha = -30$ dB. The angular spread of DMC is not modeled here, i.e. $\mathbf{R}_m^T = \mathbf{R}_m^R = \mathbf{I}$.

are 3.41° and 1.17° , respectively.

In summary, the above results demonstrated that the ESNR selection strategy is effective, and that the proposed multi-band estimator indeed achieves the CRB, as expected by the results of Fig. 5.

2) *PD-PFA performance*: Fig. 9 shows the PD-PFA performance curves. At the same PD level, our combined multi-band estimator has a significantly lower PFA compared to any of the single-band estimators on the constituent sub-bands. This is mainly because our combined multi-band estimator can resolve the grating lobes effect caused by angular ambiguity. For example, at a PD of 0.97, our proposed combined multi-band estimator achieves a PFA of about 0.16, while the PFA for the constituent 8.75 GHz and 21.7 GHz sub-bands are 0.31 and 1, respectively. At a PD of 1, the PFA for our combined multi-band estimator is about 5.86×10^{-3} , while that for the constituent 8.75 GHz and 21.7 GHz sub-bands are at least 0.067 and 1, respectively. This translates to a $27.00\times$ reduction

in PFA for our proposed combined multi-band algorithm, compared to only a $4.67\times$ reduction and no reduction for the 8.75 GHz and 21.7 GHz single-band estimators, respectively, given a $1.03\times$ increase in PD from 0.97.

Connecting with the results shown in Fig. 8, although the single-band estimator on the 21.7 GHz sub-band gives a reasonably good AoD RMSE in the CRB-achieving region, that performance cannot guarantee a truthful recovery of the sensing environment due to its high PFA. Our combined multi-band estimator, however, can resolve this issue, underscoring the need for multi-band even when RMSE improvements are marginal.

In summary, the above results demonstrated that the strategy of matching across sub-bands by the Hungarian algorithm for reducing angular ambiguity due to the grating lobes effect is effective, as the proposed multi-band estimator achieves a significantly lower PFA at the same PD level compared to the single-band estimators on the constituent sub-bands.

VI. CONCLUSIONS AND FUTURE WORK

This paper investigated multi-band sensing in FR3 ISAC systems in the presence of background DMC, focusing on how frequency-dependent propagation effects fundamentally alter sensing performance. A novel multi-band ISAC system model incorporating sub-band frequency-dependent background DMC was analyzed using CRB-based fundamental sensing limits and modified Cassini ovals, revealing how conventional, linear intuitions on sensing drawn from SC-only models do not necessarily hold, and also how multi-band sensing performance gains in localization accuracy and detection probability may manifest, in DMC-dominated scenarios. To operationalize these insights, a scalable, CRB-achieving multi-band estimation framework was proposed that combines single-band estimates while resolving angular ambiguities caused by grating lobes.

Specifically, the PDP analysis illustrated the trade-off between higher SC signal power and DMC interference power as sub-band frequencies decrease. The modified Cassini ovals showed that at higher sub-band frequencies, a concentrated DMC angular profile may result in improvements of sensing performance as the scatterer moves away from the LoS path. The CRB analysis showed that one sub-band may not dominate sensing performance across all SNR levels and revealed a DMC-dominated region at high SNR, with only minor CRB improvements as power increases. It also showed that, given dB-domain reductions in the DMC power ratio, there are consistent drops in CRB on a logarithmic scale. The ESNR analysis showed how the sub-bands can “help each other” in a multi-band system. Finally, the RMSE and PD-PFA simulation results demonstrated that the proposed multi-band estimator achieves near-fundamental limit performance in the CRB-achieving regime and provides substantial accuracy gains and reductions in the false alarm rate over single-band estimators. In a representative scenario, delay estimation errors were reduced by 37.41% and 17.04% compared to single-band processing at 8.75 GHz and 21.7 GHz, respectively.

Overall, this work establishes the critical role of background DMC modeling in multi-band ISAC for future 6G applications,

providing both theoretical and algorithmic foundations for understanding and exploiting multi-band trade-offs in FR3 systems.

For future work, we plan to use the proposed framework in upcoming measurement campaigns to verify the multi-band estimator’s capabilities practically and to explore the role of each sub-band in multi-band sensing. We also plan to investigate the effects of the angular distribution of DMC, as well as the case in which the covariance matrices of the noise and DMC interference are unknown. Additionally, we plan to develop a joint multi-band algorithm that achieves the exact CRB.

ACKNOWLEDGMENTS

This work is supported by Tamkeen under the Research Institute NYUAD grant CG017.

APPENDIX A DERIVATIONS OF THE MINIMAL VARIANCE LINEAR UNBIASED ESTIMATOR

For notational simplicity, in this appendix, we consider the case of some general location parameter ψ estimated across sub-bands $m = 1, 2, \dots, M$. We can write the estimate per sub-band as a random variable $\hat{\psi}_m \sim \mathcal{N}(\psi, \sigma_m^2)$. We want to design the weights $\{w_m\}_{m=1}^M$ for the linear estimator $\hat{\psi} = \sum_{m=1}^M w_m \hat{\psi}_m$.

Our objective is to minimize the mean squared error (MSE). But since the estimator is unbiased, the sum of weights should be 1, and the objective function is equivalently the variance of $\hat{\psi}$. In other words, we can write a problem:

$$(\mathcal{P}_{\text{MVLUE}}) : \begin{cases} \min_{w_{1:M}} & \text{var}(\hat{\psi}) = \sum_{m=1}^M w_m^2 \sigma_m^2 \\ \text{s.t.} & \sum_{m=1}^M w_m = 1. \end{cases} \quad (51)$$

The Lagrangian is convex with

$$\mathcal{L}(w_{1:M}, \lambda) = \sum_{m=1}^M w_m^2 \sigma_m^2 + \lambda \left(\sum_{m=1}^M w_m - 1 \right), \quad (52)$$

where λ is the Lagrangian multiplier. Hence, it is evident that we want

$$\frac{\partial \mathcal{L}}{\partial w_m} = 2\sigma_m^2 w_m + \lambda = 0, \forall m, \quad (53)$$

which solves to $w_m \propto 1/\sigma_m^2$. Substituting the constraint for obtaining an unbiased estimator, we get

$$w_m = \frac{\sigma_m^{-2}}{\sum_{m=1}^M \sigma_m^{-2}}. \quad (54)$$

For unbiased estimators, CRB is equivalently the lower bound of the variances. So when the individual estimators $\hat{\psi}_m$ are efficient, we can substitute σ_m^2 with our estimated value: $\text{CRB}_{\hat{\psi}_m}$, obtaining (42). Since our estimated CRBs has extra randomness, we can substitute the actual $\text{CRB}_{\psi, m}$ in place of σ_m^2 to obtain a reliable lower bound for the combined multi-band estimator, which we call *approximate CRB* as in (31).

REFERENCES

- [1] Z. Tao, W. Xu, and X. You, "Provable Performance Bounds for Digital Twin-Driven Reinforcement Learning in Wireless Networks: A Novel Digital-Twin Bisimulation Metric," *IEEE Transactions on Signal Processing*, vol. 73, pp. 4430–4445, 2025.
- [2] X. Wang, Q. Zhang, N. Cheng, J. Chen, Z. Zhang, Z. Li, S. Cui, and X. Shen, "RadioDiff-3D: A 3D×3D Radio Map Dataset and Generative Diffusion Based Benchmark for 6G Environment-Aware Communication," *IEEE Transactions on Network Science and Engineering*, vol. 13, pp. 3773–3789, 2026.
- [3] M. Chafii, L. Bariah, S. Muhaidat, and M. Debbah, "Twelve Scientific Challenges for 6G: Rethinking the Foundations of Communications Theory," *IEEE Communications Surveys & Tutorials*, pp. 1–1, 2023.
- [4] R. Liu, L. Zhang, R. Y.-N. Li, and M. Di Renzo, "The ITU Vision and Framework for 6G: Scenarios, Capabilities, and Enablers," *IEEE Vehicular Technology Magazine*, 2025.
- [5] F. Liu, Y. Cui, C. Masouros, J. Xu, T. X. Han, Y. C. Eldar, and S. Buzzi, "Integrated sensing and communications: Toward dual-functional wireless networks for 6g and beyond," *IEEE journal on selected areas in communications*, vol. 40, no. 6, pp. 1728–1767, 2022.
- [6] N. González-Prelcic, M. F. Keskin, O. Kaltiokallio, M. Valkama, D. Dardari, X. Shen, Y. Shen, M. Bayraktar, and H. Wymeersch, "The integrated sensing and communication revolution for 6g: Vision, techniques, and applications," *Proceedings of the IEEE*, vol. 112, no. 7, pp. 676–723, 2024.
- [7] A. Bazzi and M. Chafii, "Designing Waveforms with Adjustable PAPR for Integrated Sensing and Communication," in *ICC 2025 - IEEE International Conference on Communications*, 2025, pp. 6633–6638.
- [8] S. Naoumi, A. Bazzi, R. Bomfin, and M. Chafii, "Deep Learning-Enabled Angle Estimation in Bistatic ISAC Systems," in *2023 IEEE Globecom Workshops (GC Wkshps)*, 2023, pp. 854–859.
- [9] —, "High-Resolution Sensing in Communication-Centric ISAC: Deep Learning and Parametric Methods," *IEEE Journal on Selected Areas in Communications*, vol. 44, pp. 2201–2216, 2026.
- [10] A. Bazzi, R. Bomfin, M. Mezzavilla, S. Rangan, T. S. Rappaport, and M. Chafii, "Upper Mid-Band Spectrum for 6G: Vision, Opportunity and Challenges," *IEEE Communications Magazine*, vol. 64, no. 1, pp. 206–212, Jan. 2026.
- [11] T. S. Rappaport, D. Shakya, and M. Ying, "Point Data for Site-Specific Mid-Band Radio Propagation Channel Statistics in the Indoor Hotspot (InH) Environment for 3GPP and Next Generation Alliance (NGA) Channel Modeling," *arXiv preprint arXiv:2409.19873*, 2024.
- [12] D. Shakya, M. Ying, T. S. Rappaport, H. Poddar, P. Ma, Y. Wang, and I. Al-Wazani, "Comprehensive FR1(C) and FR3 Lower and Upper Mid-Band Propagation and Material Penetration Loss Measurements and Channel Models in Indoor Environment for 5G and 6G," *IEEE Open Journal of the Communications Society*, vol. 5, pp. 5192–5218, 2024.
- [13] F. Zhang, T. Mao, M. Li, M. Hua, J. Chen, C. Masouros, and Z. Wang, "Near-Field ISAC for THz Wireless Systems," *IEEE Network*, vol. 39, no. 6, pp. 54–61, 2025.
- [14] M. Mezzavilla, A. Dhananjay, M. Zappe, and S. Rangan, "A Frequency Hopping Software-Defined Radio Platform for Communications and Sensing in the Upper Mid-Band," in *Proc. IEEE International Workshop on Signal Processing Advances in Wireless Communications (SPAWC)*, Lucca, Italy, 2024, pp. 611–615.
- [15] T. Raviv, S. Kang, M. Mezzavilla, S. Rangan, and N. Shlezinger, "Multi-Frequency Upper Mid-Band Localization," in *Proc. IEEE International Workshop on Signal Processing Advances in Wireless Communications (SPAWC)*, 2024, pp. 736–740.
- [16] D. Wang, I. Jariwala, A. Bazzi, S. Rangan, T. S. Rappaport, and M. Chafii, "Compressed Multiband Sensing in FR3 Using Alternating Direction Method of Multipliers," accepted by *IEEE Wireless Communications and Networking Conference (WCNC)*, Kuala Lumpur, Malaysia, Apr. 2026, pp. 1–6.
- [17] Y. Wan, Z. Hu, A. Liu, R. Du, T. X. Han, and T. Q. Quek, "Ofdm-based multiband sensing for isac: Resolution limit, algorithm design, and open issues," *IEEE Vehicular Technology Magazine*, vol. 19, no. 2, pp. 51–59, 2024.
- [18] H. Li, K. Qu, C. Sun, S. Wang, X. Wang, Y. Zhang, B. Priyanto, and H. Zhang, "Multi-node multi-band cooperative integrated sensing and communications: State-of-the-art, challenges and opportunities," *IEEE Wireless Communications*, vol. 32, no. 4, pp. 180–188, 2025.
- [19] J. Hu, Z. Chen, and J. Luo, "Multi-band reconfigurable holographic surface based isac systems: Design and optimization," in *ICC 2023 - IEEE International Conference on Communications*, 2023, pp. 2927–2932.
- [20] Z. Hu, A. Liu, Y. Wan, T. Q. S. Quek, and M.-J. Zhao, "Two-stage multiband wi-fi sensing for isac via stochastic particle-based variational bayesian inference," in *GLOBECOM 2023 - 2023 IEEE Global Communications Conference*, 2023, pp. 5617–5622.
- [21] P. Testolina, M. Polese, and T. Melodia, "Sharing spectrum and services in the 7–24 ghz upper midband," *IEEE Communications Magazine*, vol. 62, no. 8, pp. 170–177, 2024.
- [22] S. Fortunati, L. Sanguinetti, F. Gini, M. S. Greco, and B. Himed, "Massive MIMO Radar for Target Detection," *IEEE Transactions on Signal Processing*, vol. 68, pp. 859–871, 2020.
- [23] A. R. Chiriyath, B. Paul, G. M. Jacyna, and D. W. Bliss, "Inner Bounds on Performance of Radar and Communications Co-Existence," *IEEE Transactions on Signal Processing*, vol. 64, no. 2, pp. 464–474, 2016.
- [24] P. Kumari, J. Choi, N. González-Prelcic, and R. W. Heath, "IEEE 802.11ad-Based Radar: An Approach to Joint Vehicular Communication-Radar System," *IEEE Transactions on Vehicular Technology*, vol. 67, no. 4, pp. 3012–3027, 2018.
- [25] R. Bomfin and M. Chafii, "Unique Word-Based Frame Design for Bistatic Integrated Sensing and Communication," *IEEE Transactions on Wireless Communications*, vol. 23, no. 12, pp. 19333–19349, 2024.
- [26] S. Jiang, W. Wang, Y. Miao, W. Fan, and A. F. Molisch, "A Survey of Dense Multipath and Its Impact on Wireless Systems," *IEEE Open Journal of Antennas and Propagation*, vol. 3, pp. 435–460, 2022.
- [27] A. Richter, J. Salmi, and V. Koivunen, "An Algorithm for Estimation and Tracking of Distributed Diffuse Scattering in Mobile Radio Channels," in *Proc. IEEE 7th Workshop on Signal Processing Advances in Wireless Communications (SPAWC)*, 2006, pp. 1–5.
- [28] M. Käske and R. Thomä, "Maximum-Likelihood-Based Estimation of Angular Parameters of Dense Multipath Components," in *Proc. 9th European Conference on Antennas and Propagation (EuCAP)*, 2015, pp. 1–6.
- [29] B. Hanssens, K. Saito, E. Tanghe, L. Martens, W. Joseph, and J.-I. Takada, "Modeling the Power Angular Profile of Dense Multipath Components Using Multiple Clusters," *IEEE Access*, vol. 6, pp. 56084–56098, 2018.
- [30] T. Jost, W. Wang, U.-C. Fiebig, and F. Perez-Fontan, "Detection and Tracking of Mobile Propagation Channel Paths," *IEEE Transactions on Antennas and Propagation*, vol. 60, no. 10, pp. 4875–4883, 2012.
- [31] K. Saito, J.-I. Takada, and M. Kim, "Dense Multipath Component Parameter Estimation in 11 GHz-Band Indoor Environment," in *Proc. IEEE 27th Annual International Symposium on Personal, Indoor and Mobile Radio Communications (PIMRC)*, 2016, pp. 1–6.
- [32] R. Bomfin, A. Rasteh, A. Bazzi, H. Guo, H. Lee, M. Mezzavilla, S. Rangan, J. Choi, and M. Chafii, "Multi-Band Channel Sensing in the Upper Mid-Band (FR3)," accepted in *IEEE Global Communications Conference (GLOBECOM) 2025*, Taipei, Taiwan, Dec. 2025.
- [33] R. Bomfin, A. Rasteh, M. Kim, H. Park, H. Guo, H. Lee, M. Mezzavilla, S. Rangan, J. Choi, and M. Chafii, "Multi-Band Integrated Sensing and Communication Channel Measurements in the FR3," accepted in *IEEE International Conference on Communications (ICC) 2026*, Glasgow, Scotland, UK, May 2026.
- [34] A. F. Molisch, "Ultra-Wide-Band Propagation Channels," *Proceedings of the IEEE*, vol. 97, no. 2, pp. 353–371, 2009.
- [35] A. Molisch, "Ultrawideband propagation channels-theory, measurement, and modeling," *IEEE Transactions on Vehicular Technology*, vol. 54, no. 5, pp. 1528–1545, 2005.
- [36] K. Haneda, A. Richter, and A. F. Molisch, "Modeling the Frequency Dependence of Ultra-Wideband Spatio-Temporal Indoor Radio Channels," *IEEE Transactions on Antennas and Propagation*, vol. 60, no. 6, pp. 2940–2950, 2012.
- [37] R. C. Qiu and I.-T. Lu, "Multipath resolving with frequency dependence for wide-band wireless channel modeling," *IEEE Transactions on Vehicular Technology*, vol. 48, no. 1, pp. 273–285, 1999.
- [38] C. A. Balanis, *Antenna theory: analysis and design*. John Wiley & sons, 2016.
- [39] Y. Huang, *Antennas: from theory to practice*. John Wiley & Sons, 2021.
- [40] A. Richter, "Estimation of Radio Channel Parameters: Models and Algorithms," Ph.D. dissertation, Dept. Elektrotechnik und Informationstechnik, Technische Universität Ilmenau, Ilmenau, Germany, 2005.
- [41] S. M. Kay, *Fundamentals of Statistical Signal Processing, Volume I: Estimation Theory*. Prentice Hall, 1993.
- [42] N. J. Willis, *Bistatic radar*. SciTech Publishing, 2005, vol. 2.
- [43] S. Merrill and E. SKOLNIK, *RADAR HANDBOOK*. McGraw Hill, 2008.
- [44] R. J. Mailloux, *Phased array antenna handbook*. Artech house, 2017.